ЖУРНАЛ ФІЗИЧНИХ ДОСЛІДЖЕНЬ
т. 6, № 2 (2002) с. 218–235

JOURNAL OF PHYSICAL STUDIES
v. 6, No. 2 (2002) p. 218–235

ON SOME PROBLEMS OF LARGE SUPERCONDUCTING MAGNETS

V. Kovachev
G. Nadjakov Institute of Solid State Physics,
Bulgarian Academy of Sciences,
BG–1784 Sofia, Bulgaria.

(Received February 7, 2002; received in final form May 7, 2002)

Following a general introduction to the subject (Section I), the first part of the present review (Section II) is devoted to uncertainties of analytical and numerical analyses of energy dissipation in superconducting accelerator magnets working at relatively high ramp rate. The loss experimental techniques are discussed as well as the source of error in the measurements. The correlation between the interstrand resistance of Rutherford structures and quench current behaviour of superconducting magnets are considered. In the second part of this review (Section III) some important problems of the cooling of insertion quadrupoles for Large Hadron Collider (CERN) are presented. Experimental results below 2 K are interpreted by possible self-sustained pumping based on quantum-mechanical fountain effect in superfluid ^{4}He.

Key words: superconductivity, superconducting magnets, AC losses, heat transfer.

PACSnumber(s): 85.25.Ly, 85.25.Wh

I. INTRODUCTION

Many previous century discoveries in superconductivity are still important subject for physics research and this tendency will proceed probably for years to come. Unfortunately, application of such unique and very useful from industrial point of view phenomenon like superconductivity is not very wide so far but for some periods of enthusiasm (in the 60s and 70s after the development of A–15 materials) or real euphoria (after the discovery of HTS). These days's people are learning to believe that the new class borum superconductors or very recently discovered high-temperature C_{60} superconductors will have a bright application future. According to our experience, however, it is too early to predict.

In fact superconductivity at present is used as real commercial application on a limited number of occasions: telecommunication filters, small energy storages, superconducting magnets for MRI. There are some other projects for large scale application of superconductivity like: levitation transport, large utility system energy storages, transmission lines, current limiters, etc., which sometimes are very active but from time to time die out due to lack of interest and funds.

A real large-scale high current/high magnetic field application of superconductivity is magnets for modern accelerator physics, high energy physics, and thermonuclear fusion research. This is, however, a situation when science works for science, not for industry. Nevertheless, making superconducting magnets for high power accelerators (colliders) and thermonuclear fusion devices is very useful because apart from other better properties it saves a lot of energy which in practice makes development of such huge machines visible (Superconducting Supercollider, Large Hadron Collider, International Thermonuclear Experimental Reactor, Large Helical Device) and much cheaper for the society.

The aim of this work is to address specific problems of superconducting accelerator magnets. Those problems make properties of a particular magnet unacceptable. They also cause a significant spread of magnet characteristics when a large number of magnets must be produced (approximately 10 000 were needed for the Superconducting Supercollider main ring). In other words, each magnet becomes more or less a unique one which makes it difficult for the accelerator to operate.

Generally speaking, besides some technological problems of making superconducting magnets, many problems of high current/high field application of superconductivity arise from the properties of superconducting material used. That is why any large project of application of superconductivity requires specific program for development of particular superconducting materials that are usually commercially available but not suitable for a particular application. Basically, superconducting material besides high critical parameters or a particular combination of two of them should posses good enough mechanical properties, low level of AC losses in case of alternating field or current, etc. Unfortunately, the only material widely used at present for building large magnets is the NbTi alloy made almost 50 years ago. This is because NbTi has relatively high critical current and field at 4 K, good mechanical properties and ductility, available metallurgical methods for massive production of long wires and different technologies for making multifilamentary wires with micron and submicron size filaments. There are also various techniques available for limiting the induced currents into the copper matrix of NbTi conductors, methods for adjusting the RRR, etc. It is curious to mention that A–15 materials (Nb_3Sn and Nb_3Ge for instance) developed in the 60s and 70s are still not very suitable for magnet application due to poor mechanical properties of A–15s with their better than NbTi critical current and field at 4 K. Requirements for a higher field of magnets are fulfilled so far using NbTi and lowering the operational temperature down to $1.8 \div 1.9$ K. This allows to increase the critical current density of NbTi, achieve higher field and avoid the application of Nb_3Sn (Large Hadron Collider (LHC) under development at CERN). Speaking of high temperature superconductors (HTS) besides very intensive effort to develop good high current/high field material the goal has not been achieved yet. There are some projects at present, however, to develop pretty long YBCO tape based on stainless steel substrate with a critical current density of 1 MA/cm^2 at 77 K and $4 \div 5$ T. This kind of properties obviously will be good enough for some power application of HTS in near future.

The problems of application of superconductivity in our opinion have not just technical background but also pure psychological one. On many occasions superconducting power devices are smaller in size, with higher efficiency, equal or cheaper in price but they have not been accepted by the industry. This could be explained by some conservative traditions in production and trade business and a lack of trust in modern cryogenics and superconductivity devices for a reliable operation. Unfortunately, such conservatism always exists in the society against something revolutionary new. A typical example of it is the story of the power transmission line project of Brookhaven National Laboratory (BNL), USA [1]. The Advanced Technology Division of BNL developed and built a 100 m superconducting AC power transmission line (1 GW three phase power) in the late 70s and early 80s, and comprehensively tested it. The project was very successful demonstrating wonderful behaviour of superconductivity at any fault conditions like an overload, higher voltage, cryogenic refrigerator fault, etc. Nevertheless, the project was "frizzed out" and not taken from the utility companies besides that several projects for utilizing such a line in the Long Island, the New York City and the State of Pennsylvania have been officially considered.

In some cases, however, traditional technologies remain very cheap which must be taken as a main obstacle for application of superconductivity. This is basically the situation with superconducting electronics and widely used so far semiconducting silicon technology, in particular.

II. ENERGY DISSIPATION IN SUPERCONDUCTING ACCELERATOR MAGNETS

A. Analysis and losses calculation

As was mentioned above, energy dissipation could be a problem in superconducting accelerator magnets when the magnetic field/current ramp rate is relatively high (in order of 0.1 T/s, 100 A/s or higher). This was the case with dipole magnets (DM) for High Energy Booster (HEB) for the Superconducting Supercollider (SSC) Project [2, 3]. Below we are going to consider how the analysis of AC loss in such magnets could be carried out, which are major sources of loss, uncertainties in its calculation, major sources of error in loss calculation, etc. Experimental techniques of loss measurements of short superconducting samples of Rutherford cables and model dipole magnets are also discussed. Some more detailed consideration is given to the electric method for AC loss measurements in magnets at 4 K. The calorimetric method used in superfluid helium below 2 K is also considered.

A major source of energy dissipation in the superconductor of an accelerator dipole (HEBDMs of SSC are taken as an example) is the magnetization hysteresis in the superconducting filaments, intrastrand (wire matrix) coupling current losses, interstrand (Rutherford cable) coupling current loss, and sometimes in the case of very thin filaments — proximity effect losses in the matrix between filaments.

The hysteresis in the filaments produces a loss which does not depend on the frequency or ramp rate of the magnetic field or transport current. Losses are given by the magnetization hysteresis loop [$M = f(B)$] area.

The intrastrand coupling through the cooper matrix is a source of eddy current type of losses that depend on the field/current ramp rate. These losses enlarge the area of the magnetization loop depending on the ramp during the field/current cycle. If the ramp is constant during the cycle, the increase of the loop area will be uniform throughout the cycle (at any B of the cycle). In order to limit intrastrand induced currents and loss, a high resistivity CuNi barriers can be introduced around the filament bundles. This kind of technology is widely used for relatively high frequency multifilamentary superconductors.

The interstrand coupling in the Rutherford cable creates another component of eddy current type loss that depends on the ramp rate and again increases the magnetization loop area. To establish a real value of interstrand currents is not an easy task and we are going to discuss it later on. We will only mention here that in order to control the level of interstrand resistance people try to choose proper conditions of coil curing or cover the conductor with an oxide layer (ebanol, for instance) or by a special alloy (Sn + 5% Ag).

In some multifilamentary superconductors with fairly small filament diameter the interfilament spacing becomes equal or smaller than the doubled coherent length of the superconductor. In this case a weak induced superconductivity (proximity effect) can exist in the normal metal matrix. The induced superconductivity between filaments can make AC behaviour at low field like the "monofilament" one which obviously enlarges the loss near $B = 0$. This can cause a sharp increase of hysteresis loop area near zero field which like the magnetization loss of filaments does not depend on the ramp rate or frequency. At higher field the loss increase becomes nonessential because the proximity effect diminishes quickly with the field. To avoid the proximity effect loss increase submicron filament technology of superconductors for AC application introduces a small amount of ingredients (Ni, Mn) in order to reduce the matrix RRR and limit the proximity effect. Mn is considered a very effective scattering material because Mn atoms cause a flip-flop of the spin of conducting electrons and very small amounts of Mn (0.5wt%) can make substantial reduction of RRR.

The average of the bipolar cycle magnetization power hysteresis loss in the superconductor is given by a double integral over entire induction range and entire volume of the magnet coil:

$$\langle W_{\mathrm{h}}^{\mathrm{sc}}\rangle = \frac{\lambda}{2\mu_0 T_{\mathrm{r}}}\int\int M\,dB\,dV\ , \tag{1}$$

where λ is the ratio of the superconductor cross section to the entire cross section of multifilamentary superconductor, μ_0 is the magnetic permeability of vacuum, T_r is the time of field/current ramp up from 0 to $B_{\max}$ or down from $B_{\max}$ to 0, M is the magnetic moment, B is the magnetic induction, V is the total volume of stabilized multifilamentary superconductor.

Losses can be calculated both analytically and numerically using simple critical state formulas because filaments of approximately 10 μ in diameter are fully penetrated by magnetic flux at low induction of about 500 G. In other words, at all fields of interest we have a full penetration of flux. It must be noted that both methods give results pretty closed to experimentally obtained filament magnetization losses. For analytical calculation the magnetization is given by

$$M = \frac{2}{3\pi}\mu_0 J_{\mathrm{c}} d_{\mathrm{f}}\ , \tag{2}$$

where J_{c} is the critical current density in the filaments, and d_{f} is the filament diameter.

According to the Kim–Anderson critical state model [4]

$$J_{\mathrm{c}} = \frac{2J_{\mathrm{c}}(B_0)B_0}{B+B_0}\ , \tag{3}$$

where B_0 and $J_{\mathrm{c}}(B_0) = J_{\mathrm{c}0}/2$ are material constants.

The analytical method uses a linear distribution of magnetic induction across the magnet coil where the local maximum induction achieved during a ramp cycle varies from B_1 to B_2.

Thus, after integration the resulting average power loss is

$$\langle W_{\mathrm{h}}^{\mathrm{sc}}\rangle = \frac{4\lambda V}{3\pi T_{\mathrm{r}}} d_{\mathrm{f}} \frac{J_c(B_0)B_0^2}{B_2-B_1}\left\{\frac{B_2+B_0}{B_0}\left[\ln\left(\frac{B_2+B_0}{B_0}\right)-1\right] - \frac{B_1+B_0}{B_0}\left[\ln\left(\frac{B_1+B_0}{B_0}\right)-1\right]\right\}\ . \tag{4}$$

The numerical method is a little more accurate and gives results closer to the experimental data. In order to gain accuracy the influence of the transport current on the magnetization is taken into account. The magnetic moment becomes

$$M = \frac{2}{3\pi}\mu_0 J_{\mathrm{c}} d_{\mathrm{f}}\left(1-\frac{J}{J_c}\right)\ ,$$

where J is the transport current density.

Also the computed nonlinear distribution of magnetic field throughout the coil cross section is used. The situation with the intrastrand coupling losses is quite similar in terms that both the analytical and the numerical calculations of losses are close to the experimentally measured ones providing use of correct RRR of the matrix.

The analytical method uses the linear distribution of magnetic induction. The following integral over the total coil volume gives loss power:

$$\langle W_{\mathrm{e}}^{\mathrm{st}}\rangle = \frac{\mu_0}{\rho_{\mathrm{et}}}\left(\frac{L}{2\pi}\right)^2\int\left(\frac{\partial B}{\partial t}\right)^2 dV = \frac{2V}{3\mu_0}\frac{B_2^3-B_1^3}{B_2-B_1}\frac{\tau}{T_{\mathrm{r}}^2} \tag{5}$$

with

$$\tau = \frac{\mu_0}{2\rho_{\mathrm{et}}}\left(\frac{L}{2\pi}\right)^2\ ,$$

and

$$\rho_{\mathrm{et}}^{-1} = \frac{1}{\rho_{\mathrm{t}}} + \frac{w}{a\rho_{\mathrm{m}}} + \frac{aw}{\rho_{\mathrm{m}}}\left(\frac{2\pi}{L}\right)^2\ .$$

Here $\rho_{\mathrm{t}} = (1+\lambda)/(1-\lambda)$ is the transverse resistivity in the high contact resistance limit [5], w is the thickness of the cooper jacket of multifilamentary conductor, a is the filament bundle radius of multifilamentary conductor, ρ_{m} is the normal metal resistivity at given temperature and field, i.e., including magnetoresistivity part, L is the twist pitch length of the strand.

The numerical method uses experimental data for intrastrand coupling current magnetization of particular conductor. Power losses in the magnet coil are given by an integral over entire coil volume:

$$\langle W_{\mathrm{e}}^{\mathrm{st}}\rangle = 2\int \tau^{\mathrm{st}}\left(\frac{\partial B}{\partial t}\right)^2 dV\ , \tag{6}$$

where $\tau^{\rm st} = (M_{\rm e}/2B)$ is the eddy current decay time constant within the strand experimentally obtained and $M_{\rm e}$ is the measured eddy current magnetization of the multifilamentary superconductor.The numerical method of calculation of intrastrand loss is using the computed non-linear distribution of the derivative of magnetic induction.

The accurate amount of losses caused by interstrand coupling current in Rutherford cables can not be obtained analytically due to the lack of knowledge of real interstrand resistance. Assuming some reasonable interstrand resistance and using the model proposed by G. Morgan [6] for braids someone can try to estimate the interstrand coupling loss in a Rutherford cable. This approach can give very wrong result, however. The analytical or numerical method can be applied also if the interstrand coupling decay time constant for the particular cable is available. The interstrand losses become

$$\begin{aligned}\langle W_{\rm e}^{\rm st-st}\rangle &= 2\int \tau^{\rm st-st}\left(\frac{\partial B}{\partial t}\right)^2 dV \\ &= \frac{2}{3\mu_0}V(1-\lambda)\frac{B_2^3-B_1^3}{B_2-B_1}\frac{\tau^{\rm st-st}}{T_{\rm r}^2}\ , \qquad (7)\end{aligned}$$

where $\tau^{\rm st-st}$ is the interstrand eddy current decay time constant of a particular Rutherford cable. The integral above is over entire volume of magnet coil. It must be noticed that since $\tau^{\rm st-st}$ depends on number of strands in square (N^2), cable width (h), and twist pitch length in square (L^2) [6] someone can believe that knowing experimental data for similar Rutherford cable (with different number of strands or width for instance) the following scaling can be applied:

$$\tau_{\rm s}^{\rm st-st} = \tau_{\rm ex}^{\rm st-st}\frac{h}{h_{\rm ex}}\left(\frac{N}{N_{\rm ex}}\right)^2\left(\frac{L}{L_{\rm ex}}\right)^2 ,$$

where $\tau_{\rm s}^{\rm st-st}$ is the scaled interstrand coupling decay time constant for Rutherford cable under consideration, $\tau_{\rm ex}^{\rm st-st}$ is the experimentally obtained interstrand coupling decay time constant for a similar Rutherford cable, h, N, L are the parameters (as above) of the cable under consideration, and $h_{\rm ex}, N_{\rm ex}, L_{\rm ex}$ are the measured parameters of a similar Rutherford cable.

According to our experience, however, such an approach does not work properly and can produce very big discrepancy with the experimental data as we can see later on. This discrepancy obviously is a result of a variety of surface conditions of the strands and different interstrand resistance as a result. We are going to discuss how we have determined that fact further on.

The magnetization hysteresis in the yoke material could be another major source of energy dissipation in superconducting accelerator magnets. Losses of yoke magnetization are given as a double integral over entire induction range and entire volume of the magnet yoke:

$$\langle W_{\rm y}\rangle = \frac{1}{2\mu_0 T_{\rm r}}\int\int M\,dB\,dV\ . \qquad (8)$$

Here problems could arise when someone tries to calculate dissipation for monopolar cycle (current/field change from zero up and down to zero only). The problem actually comes from the fact that magnetization hysteresis area for monopolar cycle is not known for many magnetic materials. That is why precise calculation requires experimental measurements of monopolar magnetization of material under consideration.

Our analysis and calculation of HEBDM of SSC have shown that second order effects of energy dissipation can be considered as follows:

- Proximity effect coupling (after reduction of matrix RRR by adding 0.5wt%Mn as ingredient to the cooper).
- Transport current distribution effects.
- Flux penetration through the filament saturated layer.
- Eddy currents in the yoke, collar, and wedges.
- Mechanical hysteresis.

The total error in loss calculation was evaluated to be approximately 30%. This, in fact, predicted error comes from:

- Approximations used in theoretical models.
- Uncertainty in interstrand coupling and variation of RRR.
- Readjustment of $J_{\rm c}(B,T)$ experimental surface for different cables.
- Uncertainty in monopolar yoke hysteresis area.
- Neglecting the second order effects of dissipation.

The uncertainty in interstrand coupling in reality turned out to be a very large source of error due to huge variety of interstrand resistance of Rutherford cables. Experiments on short cable samples and model magnets have shown that the real dissipation can be a factor of $2\div 3$ higher than the calculated one.

B. Measurement methods

Electrical Method

The electrical method is used at temperature 4.2 K and above for both the energy dissipation in short pieces of Rutherford cables [7] and the loss measurements in magnets [8, 9]. The method for short samples of cable is based on the measurements of cycle magnetization:

$$\langle Q_{\rm scs}\rangle = \oint M\,dH\ . \qquad (9)$$

The method uses magnetic field, H, and magnetic moment, M, pick up coils arrangement. Samples should be several cable pitch length long in order to allow a proper averaging of interstrand coupling. The samples should be placed subsequently in a coil form that contains two saddle shaped coils. One of the coils is a dummy coil that permits the subtraction of the magnetizing field in a standard way. A small movable coil usually is provided to enable a more precise nilling of the background signal. The length of the sensing coils should be over one pitch length with the objective of being insensitive to end effects caused by finite sample length. The absolute sensitivity of the sensing coils could be determined by substituting a coil of wire wound on a bobbin the same size and shape as the cable sample, and measuring the response to a known current in the calibrating coil. A typical magnetization hysteresis loop of a SSC cable sample obtained at Westinghouse Science and Technology Center (WSTC) in Pittsburgh, Pennsylvania, is shown in Fig. 1. Measurements were made four times per second over the length of the cycle. The tilt of the plot (Fig. 1) is caused by an imperfect null, and is easy taken into account. It should be remarked that the area enclosed by the curve, which is of primary interest, is not affected by making this correction.

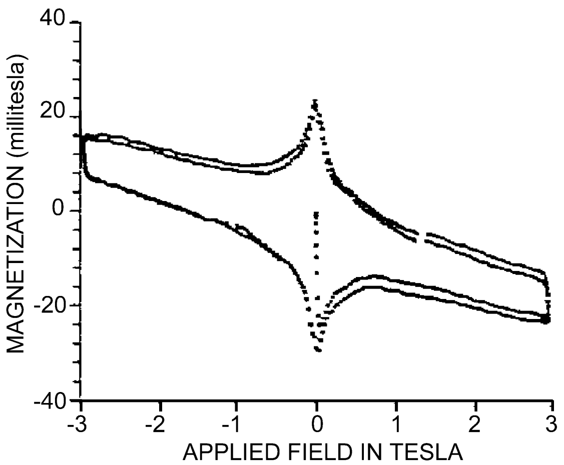

Fig. 1. Raw data of Rutherford cable magnetization, M *vs.* magnet transport current, I, as obtained for unpressurized sample at a magnetic induction ramp rate of 50 mT/s.

The failure of the hysteresis loop to close upon itself for the most part may be corrected by assuming that a small constant offset was present throughout the cycle. This typically was on the order of a tenth of a microvolt, and is probably of thermal origin. The method described above actually is a pretty standard method for magnetization measurements. The problems here could arise from the necessity of applying of $50 \div 100$ MPa prestress load on the specimen during magnetization measurements simulating the real conditions in an accelerator magnet.

Fig. 2 shows data for total energy loss per cycle per cubic meter measured for Rutherford cable. The loss of a cable made of 2.5 μ multifilamentary conductor with 0.5wt% Mn in the matrix is shown as sample 1 (squares "□" and best fit solid line). The dissipation in a cable made of 6 μ multifilamentary conductor is shown as sample 2 (circles "○" and best fit solid line). Dashed lines in Fig. 2 illustrate the estimated loss using similar equations to Eqs. (4) and (5) of this paper. The coupling losses vary linearly with the ramp rate. No difference was found for the loss per cycle for any sample when it was rotated 90 degrees, so the losses due to interstrand coupling for these samples were small compared to all other losses. In other words, the slop of the lines shown in Fig. 2 represents the intrastrand coupling loss only. This can be explained upon the fact that prestress pressure was not applied on the samples, i. e., the interstrand resistance of the cables was relatively very high. The magnetization hysteresis losses of filaments in the cables are given by the intercept of experimental lines on y-axis in Fig. 2. It can be seen clearly in Fig. 2 that intrastrand coupling of 2.5 μ conductor is substantially reduced due to adding of Mn and decrease of RRR of the cooper matrix. The effect of prestress pressure on the interstrand coupling loss is shown in Fig. 3. Obviously the prestress considerably reduces the interstrand resistance in the cable and enhances the interstrand coupling. Correspondingly, the interstrand coupling losses dissipation rises considerably (Fig. 3). Results for two different samples (pressurized and unpressurized) and two different sample positions are shown in Fig. 3. For the position perpendicular to the field measurement data are shown by the upper lines (circles and squares) and for the parallel to the field samples are shown by the lower lines (triangular and rhombic). One can see in the figure an excellent agreement for the hysteresis losses, as indicated by the y-intercepts.

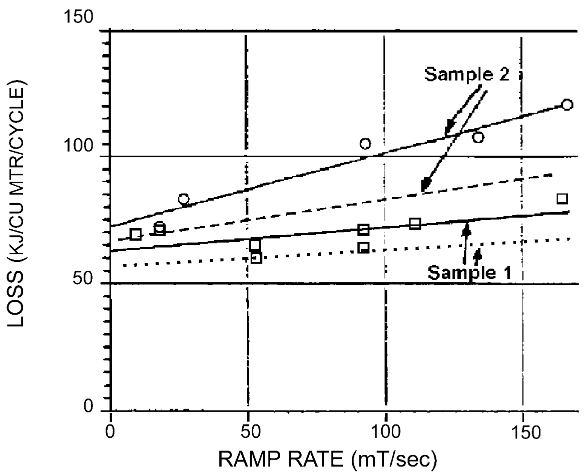

Fig. 2. Short cable sample loss per cycle *vs.* magnet induction ramp rate.

The most likely interpretation of the results shown in Fig. 3 is the following: Any interstrand coupling loss should be larger when the field is perpendicular to the cable, because much larger current loops are available for this geometry. In fact, the interstrand coupling for the parallel case can be neglected. In contrast, the intrastrand coupling losses should be isotropic in a transverse field, since the rotation of circular strand in the field should not affect the loss (the small angle due to the cable twist pitch is neglected in this argument). Thus, the entire difference between the perpendicular and parallel loss should result from the interstrand coupling.

The method for dissipation measurements in magnets is based on the fact that the energy dissipation during the cycle equals the difference between energy in and out the magnet. It must be noticed, however, that this method requires precise subtraction of two numbers that are pretty close to each other. Many problems of this method are related to the authenticity of loss number (a result of subtraction mentioned above). The loss number is usually three orders of magnitude smaller than the value of the energy in or out the magnet. That is why a calibration of the electric method is required before magnet loss measurements. We are going to discuss a possible error of measurements and the calibration method requirement later on.

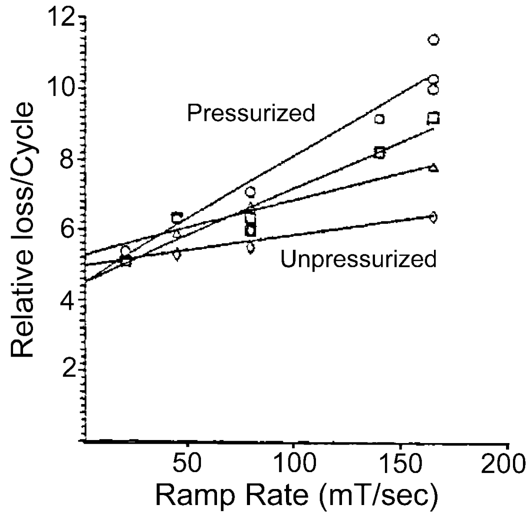

Fig. 3. Effect of prestress on dissipation in Rutherford cables.

The current ramp in accelerator magnets is linear *vs.* time (Fig. 4a). The field ramp is not exactly linear because of iron saturation but we are going to consider a linear current/field ramp for simplicity. If the superconducting magnet was an ideal inductance the voltage waveform $L(\partial I/\partial t)$ coming from the magnet would be like that shown in Fig. 4b. During the ramp, however, there is an effective resistance in the magnet due to the energy dissipation. The effective resistance is not constant and the following formula cannot be used:

$$V = L\frac{\partial I}{\partial t}\left[1 - e^{-t/\tau}\right] \ .$$

Effective resistance of magnet depends on current and magnetic field values throughout the cycle as well as on their time derivatives. The real voltage waveform $V(t)$ picked experimentally up from the magnet is like that shown in Fig. 4c. The signal obtained by subtraction of $V(t)$ and $L(\partial I/\partial t)$ is illustrated in Fig. 4d. Voltage and current integrations give the dissipation in the magnet per cycle (Fig. 5):

$$P = -\oint \left\{ \int_0^t \left[V(t) - L\frac{\partial I}{\partial t} dt \right] \right\} dI \ .$$

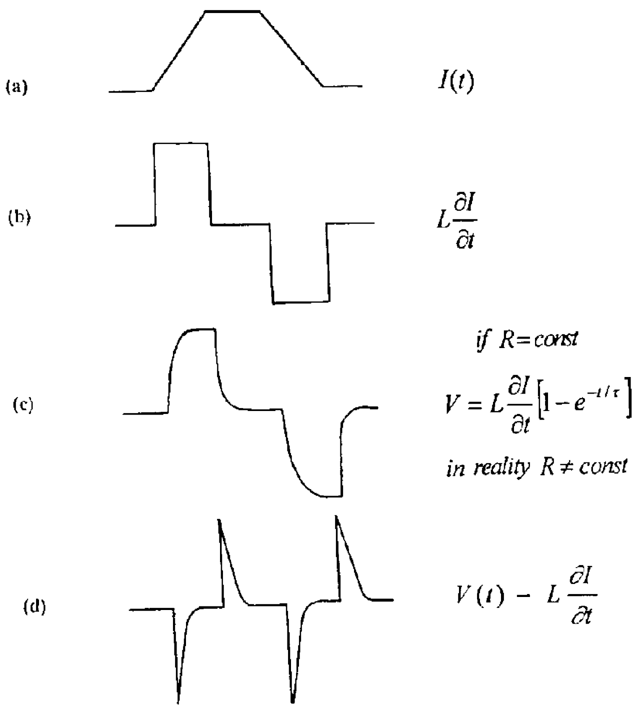

Fig. 4. Sketch of the signals of electric measurements of magnet loss: (a) the magnet current ramp *vs.* time, (b) voltage response of an ideal inductance, (c) a real magnet voltage response, and (d) the difference between $V(t)$ and $L(\partial I/\partial t)$ coming from the magnet.

The hysteresis area obtained (illustrated in Fig. 5) equals energy loss per one cycle. As was mentioned above, the electrical method requires calibration in order to secure the authenticity of the loss number obtained. The calibration is made using the following simple method. The energy dissipation of a magnet is measured in a usual way with empty magnet bore. Then a cooper bar is introduced into the magnet bore and the losses are remeasured on equal conditions of previous measurements. The difference in the measured loss gives the energy dissipation in the cooper bar and can be calculated accurately in Joules per cycle per unit length using the following formula:

$$\langle Q_c \rangle = \left(\frac{\partial B}{\partial t}\right)^2 \sigma h \left(\frac{w^3}{12}\right) T_{\mathrm{cyc}} \ , \qquad (10)$$

where σ is the average conductivity of cooper at given temperature and field throughout the cycle, h is the cooper bar height, w is the cooper bar width, $T_{\rm cyc}$ is the cycle time.

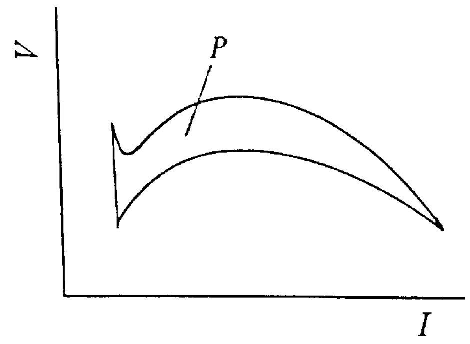

Fig. 5. Sketch of the final result of loss measurements in a superconducting magnet. Dissipation equals the area of the hysteresis in voltage, V ($V = \int_0^t [V(t) - L\frac{\partial I}{\partial t}]dt$) and current, I axis. The hysteresis area, P is obtained by closed loop integration ($P = -\oint\{\int_0^t [V(t) - L\frac{\partial I}{\partial t}]dt\}dI$).

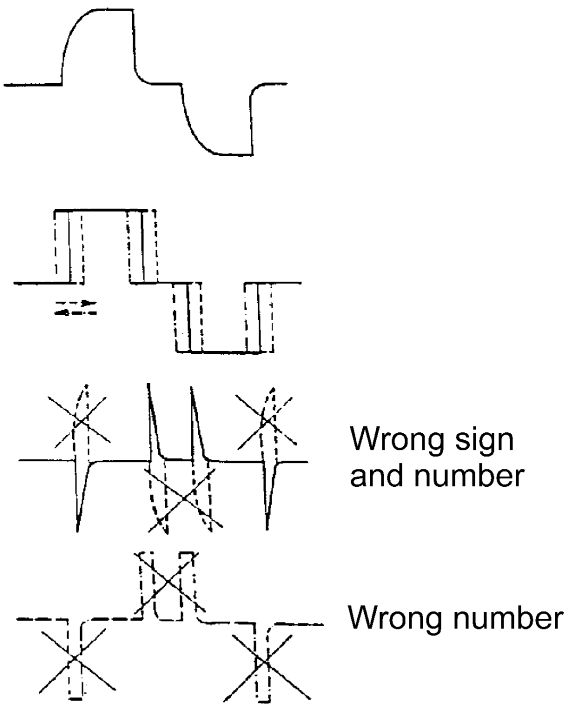

Fig. 6. Sketch of a possible loss measurement error at undesirable signals face shift. Running fast triggering of current ramp rate signal leads even to a wrong sign of loss. Running late triggering of current ramp rate signal leads to a wrong number of losses.

Another problem of electrical method for magnet dissipation measurements could be the lack of precise triggering of both $V(t)$ and $L(\partial I/\partial t)$ signals. A small phase shift error between them could lead to a completely wrong loss result. This is illustrated in Fig. 6. As shown, a phase difference can result even a wrong sign of losses which is nothing but a physically wrong result. Also a problem of electric measurements could be an offset after subtraction of $V(t)$ and $L(\partial I/\partial t)$ signals illustrated in Fig. 7. This offset can cause wrong integration result and subsequently an incorrect number for losses.

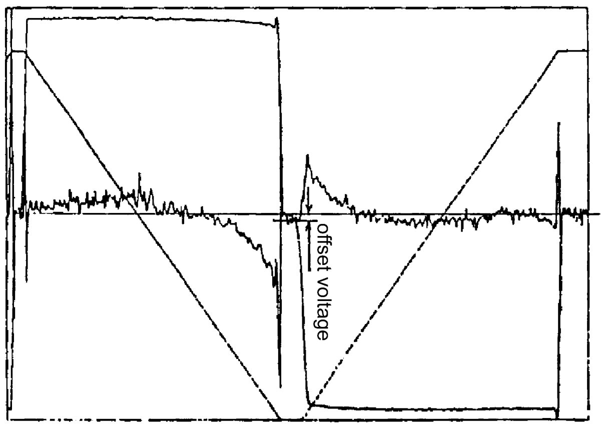

Fig. 7. Experimental signal obtained after subtraction of $V(t)$ and $L(\partial I)/\partial t)$ signals. An undesirable offset can be seen in the figure.

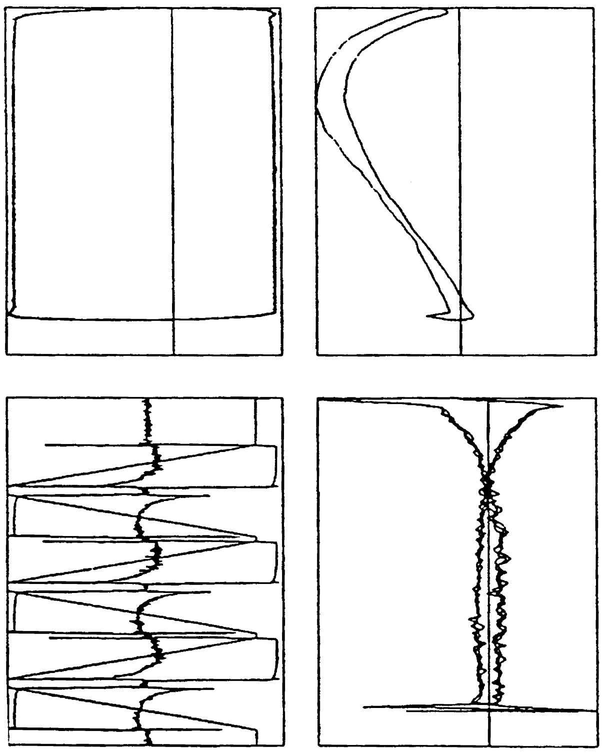

Fig. 8. Illustration of correct signals and loss result obtained on SSC model dipole at KEK, Japan.

It is not clear why this offset occurs and sometimes could be connected to a ground voltage. In order to avoid such an offset influence some people before cycle integration (see Fig. 5) make the time integral of voltage difference equal to zero. This procedure is believed in principal to be correct one, however, we recommend that it is better to avoid offset instrumental way instead of using the mathematical correction mentioned above.

Results of a correct measurement of AC losses of a short model SSC magnet performed at KEK, Japan are shown as an illustration in Fig. 8. The dissipation obtained is 155 J/cycle and the energy in and out the magnet is above 100 kJ.

C. Calorimetric Method

The calorimetric method for dissipation measurements of superconducting accelerator magnets is used at superfluid helium temperatures only. This is because the huge heat conductivity of superfluid helium permits to make correct heat balance in λ-plate cryostat and determine the loss during current/field cycle. λ-plate cryostat is a cryostat with so called λ-plate below which a test magnet is in contact with superfluid helium. The magnet is cooled in a pressurized superfluid helium at temperature usually between $1.6 \div 2.0$ K. In other words there is no temperature difference between superfluid helium and the magnet under consideration and the temperature of the magnet during test in practice immediately equals the temperature of the helium itself. The principals of measurement are given by the following simple thermodynamic considerations. The magnet under test and surrounding superfluid helium represents a thermodynamic system schematically shown in Fig. 9.

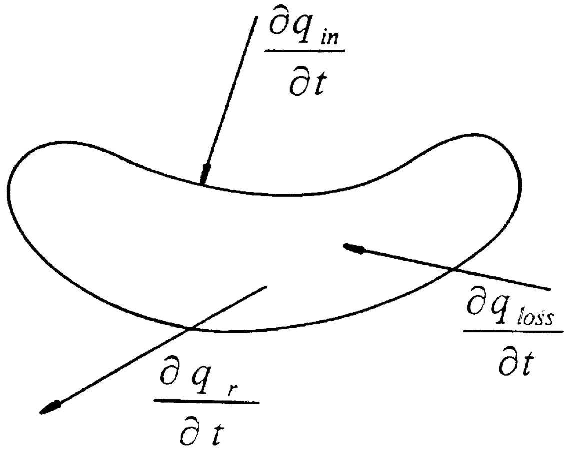

Fig. 9. Sketch of the thermodynamic system representing the magnet under test cooled by superfluid helium.

The heat power in is the heat leek due to the nonideal adiabaticity of the system $(\partial Q_{\rm in}/\partial t)$. The heat power in is also the power dissipation in the magnet under consideration $(\partial Q_{\rm loss}/\partial t)$. The heat power out is the refrigeration power $(\partial Q_{\rm r}/\partial t)$. The enthalpy difference between the start and the end of the magnet cycling is

$$\Delta H = \langle m\rangle \int_{T_i}^{T_f} \langle C(T)\rangle dT = \int_0^t \left[\frac{\partial Q_{\rm in}}{\partial t} + \frac{\partial Q_{\rm loss}}{\partial t} - \frac{\partial Q_{\rm r}}{\partial t}\right] dt \, , \tag{11}$$

where $\langle m\rangle$ is the average mass below the λ-plate in contact with superfluid helium, T_i is the initial temperature before magnet cycling, T_f is the final temperature after magnet cycling, $\langle C(T)\rangle$ is the average heat capacity of everything in contact with superfluid helium (magnet, helium itself, etc.). Because the temperature increase is very small one, $T_i \approx T_f$, i.e., $\langle mC\rangle$ can be considered constant. Thus

$$\langle m\rangle \int_{T_i}^{T_f} \langle C(T)\rangle \, dT = \langle mC\rangle \Delta T \, . \tag{12}$$

Substituting (12) in (11) we obtain

$$\frac{\langle mC\rangle \Delta T}{\Delta t} = \frac{\partial Q_{\rm in}}{\partial t} + \frac{\partial Q_{\rm loss}}{\partial t} - \frac{\partial Q_{\rm r}}{\partial t} \, . \tag{13}$$

If we switch the refregerator off just before the magnet cycling Eq. (13) becomes

$$\frac{\langle mC\rangle \Delta T}{\Delta t} = \frac{\partial Q_{\rm in}}{\partial t} + \frac{\partial Q_{\rm loss}}{\partial t} \, . \tag{14}$$

In order to determine losses we need to eliminate $\partial Q_{\rm in}/\partial t$ from Eq. (14). This can be done by means of system calibration with the known heat power pulse. Using a heater we can introduce heat pulses to the pressurized helium $\partial Q_{\rm h1}/\partial t$ and $\partial Q_{\rm h2}/\partial t$. Then

$$\langle mC\rangle = \left(\frac{\partial Q_{\rm in}}{\partial t} + \frac{\partial Q_{\rm h1}}{\partial t}\right)\left(\frac{\Delta t}{\Delta T}\right)_1 = \left(\frac{\partial Q_{\rm in}}{\partial t} + \frac{\partial Q_{\rm h2}}{\partial t}\right)\left(\frac{\Delta t}{\Delta T}\right)_2 \, , \tag{15}$$

where $(\Delta t/\Delta T)_1$ and $(\Delta t/\Delta T)_2$ are the ratios of time and temperature increases during the first and second heat pulses, respectively.

From Eq. (15) we can obtain $\partial Q_{\rm in}/\partial t$:

$$\frac{\partial Q_{\rm in}}{\partial t} = \frac{(\partial Q_{\rm h2}/\partial t)\,(\Delta t/\Delta T)_2 - (\partial Q_{\rm h1}/\partial t)\,(\Delta t/\Delta T)_1}{(\Delta t/\Delta T)_1 - (\Delta t/\Delta T)_2} \, . \tag{16}$$

After the replacement of (16) into (14) we get for the power dissipation in the magnet under test:

$$\frac{\partial Q_{\rm loss}}{\partial t}=\frac{\langle mC\rangle}{(\Delta T/\Delta t)}\frac{(\partial Q_{\rm h2}/\partial t)\,(\Delta t/\Delta T)_2-(\partial Q_{\rm h1}/\partial t)\,(\Delta t/\Delta T)_1}{(\Delta t/\Delta T)_1-(\Delta t/\Delta T)_2}\,. \tag{17}$$

The calorimetric dissipation measurement actually includes a simple measurements of temperature of pressurized superfluid helium (by an accurate carbon glass resistance (CGR) thermometer for instance) and time during magnet cycling. However, it must be noticed that this method requires λ-plate cryostat and a large refrigeration power. The method is pretty time consuming one. A sketch of obtained plot as a result of calorimetric measurements is given in Fig. 10. The temperature of the system below the λ-plate increases (resistance of CGR thermometer decreases) upon time without any dissipated power because of non-ideal adiabaticity of the system (Fig. 9).

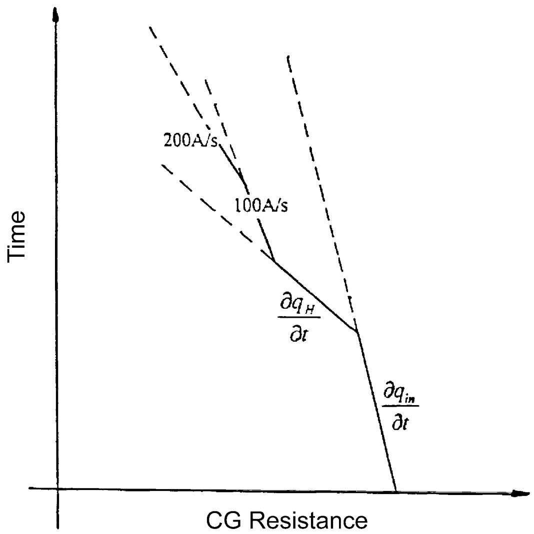

Fig. 10. Sketch of the plot obtained as a result of a calorimetric magnet loss measurement in superfluid helium.

After introducing a heater power or energizing the magnet with a certain ramp rate the slop of the line CGR(t) is changing. The calibration of the system, i. e., determination of the slop of the line experimentally obtained can be done as explained above. Experimental data of energy dissipation power per cycle in a SSC model magnet obtained by means of electrical method at 4.2 K (full circles and upper line) and by calorimetric method at 1.8 K are shown in Fig. 11. The model magnet was made using multifilamentary NbTi strand with 2.5 μ filament diameter and 0.5wt% Mn in the cooper matrix. The lower solid line represents the estimated loss using Eqs. (4)–(7). The open circles present data from calorimetric measurements of dissipation at superfluid helium temperatures. While agreement in dissipation is fairly good at rates of about $250 \div 300$ A/s the calorimetric data deviate from electric measurements at relatively low ramp rate. This deviation is probably due to higher critical current density at lower temperature (1.8 K instead 4.2 K) causing higher magnetization loss in the filaments at 1.8 K.

As we have indicated at the beginning of the present paper the dissipation measurements in SSC model magnets have manifested that experimental magnetization and intrastrand coupling losses were pretty close to the calculated ones. However, interstrand coupling dissipation was away off in some magnets. Experimental data were by a factor of $2 \div 3$ higher than calculated values. Furthermore, it appeared to be two different type of behaviour of quench current of magnets *vs.* current/field ramp rate as shown in Fig. 12.

At one of them quench current stays almost constant at low ramp rates and then goes down quickly at higher rates (type A). Another type of magnets shows degradation of quench current at low ramp rates and then some sort of plateau *vs.* the ramp rate (type B). We have made considerable efforts to find out what was the reason for that kind of behaviour and what shall be done to avoid such magnet characteristics [10–18]. It was found at first that the basic reasons for very high experimental loss were Rutherford cable characteristics, not individual strand properties (strand RRR for instance). Then it was also found that the coil curing at high pressure and temperature could lead to a very low interstrand resistance in cables. To determine that a specific method for measuring the variety of strand-to-strand resistances *in situ* in the coil after magnet autopsy was developed [10–13].

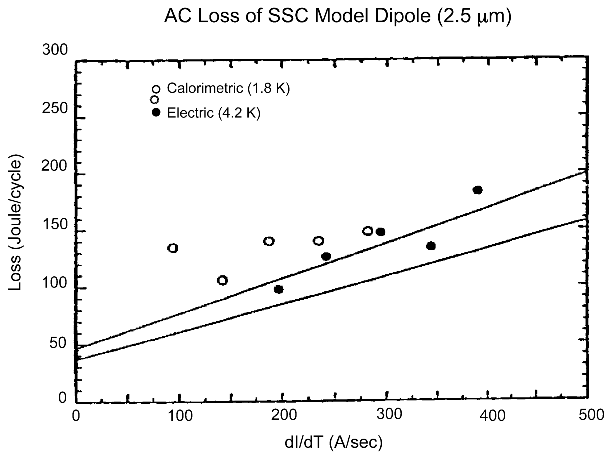

Fig. 11. Comparison between electric (at 4.2 K) and calorimetric (at 1.8 K) loss measurements of a SSC model magnet.

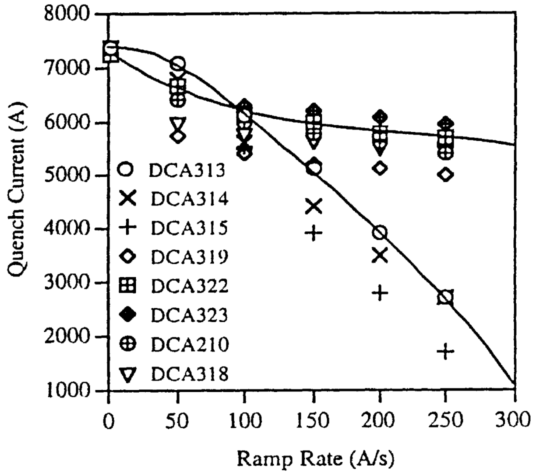

Fig. 12. Illustration of different types of behaviour of quench current *vs.* ramp rate for SSC model magnets.

In situ measurements are discussed in details in [10–13]. We are going to allude briefly here the main findings. There are several types of interstrand resistances in Rutherford cables: crossover contacts of non-adjacent strands, side-by-side contacts of adjacent strands, and roll over contact of adjacent strands. The *in situ* method and models for interpreting the experimental data can distinguish all of them and which is very important are able to determine individual strand-to-strand resistance of different kind beside a huge number of primary, secondary, and other high order parallel contacts in a cable. Because of many parallel loops strand-to-strand resistance in Rutherford cables can be very low at the quench locations of the coil (of the order of 10 nΩ) as shown in Fig. 13 for a SSC model dipole. The quench locations in the magnet coil were experimentally found prior to magnet autopsy by quench detection technique. One can see in Fig. 13 that the strand-to-strand resistance is not uniform among coil turns and can vary considerably.

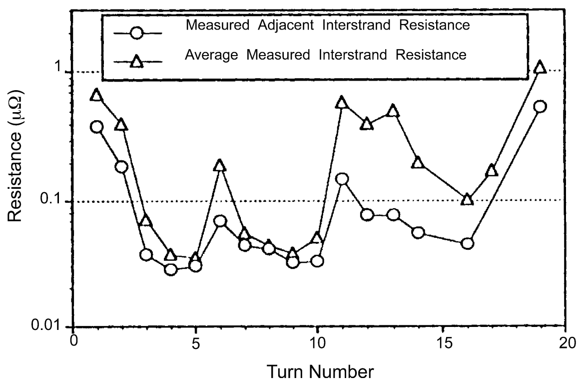

Fig. 13. Measured interstrand resistance in SSC model magnet.

The *in situ* results of strand-to-strand resistance have found reasons why quench locations are moving toward the central plane of magnet coil upon the ramp rate increase. This obviously happens because turns near midplane are exposed much stronger to dipole field $\partial B/\partial t$ due to a larger loop area of interstrand coupling leading to a higher local interstrand dissipation, local overheat and subsequent magnet quench. We show in Fig. 14 another illustration of good agreement between direct *in situ* measurements of crossover resistances and those estimated indirectly before magnet autopsy from experimental data for field quality (high harmonic field measurements) during current/field ramp.

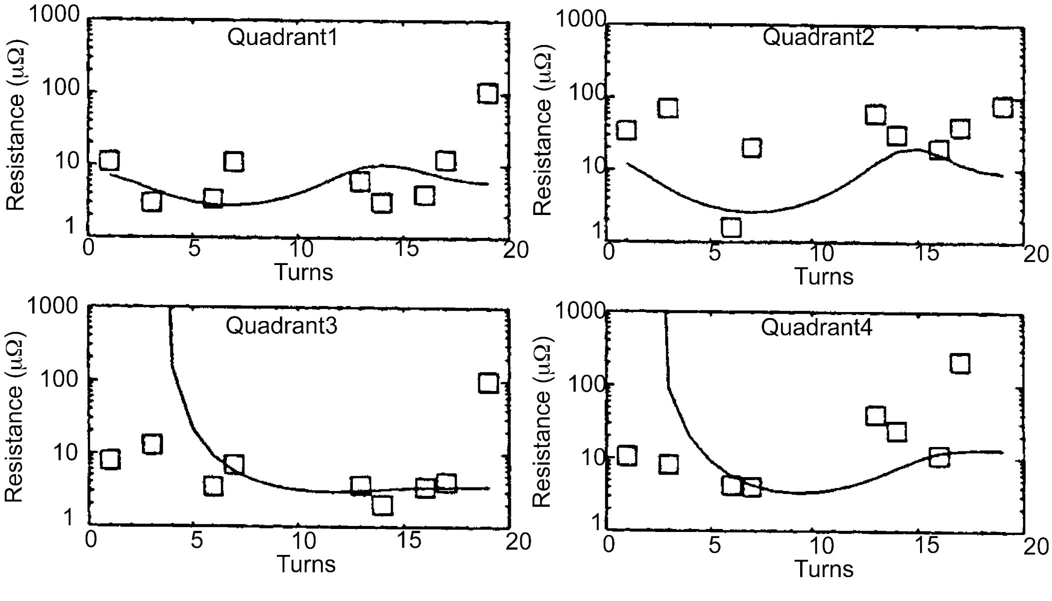

Fig. 14. Crossover interstrand resistance of a SSC model magnet obtained by direct *in situ* measurements (open squares) and by fitting field quality results measured during ramp rate (solid line).

The open squires show *in situ* data of individual crossover resistance in a SSC HEB model magnet. Solid lines represent fitted resistance from field quality measurements for the same positions of the magnet coil.

We also found that low interstrand resistance in Rutherford cables is a basic reason for type A and type B characteristics of quench current behaviour of magnets [9, 15–17]. Briefly, the A type is due to low crossover resistance all over the dipole coil that causes high interstrand coupling dissipation and quench at locations which move from the dipole pole to the midplane with ramp rate increase. The type B quench behaviour is due to some "weak" spots in the coil having low crossover resistance of the cable. As a result, induced cable currents with a large time constant can cause quench of curtain strands leading to a total quench and type B behaviour of quench current *vs.* ramp rate.

D. Section II conclusions

- The major source of energy dissipation in superconducting accelerator magnets are magnetization hysteresis of filaments, intrastrand coupling, interstrand coupling, and magnetization of iron yoke. The interstrand coupling in Rutherford cables can be a major source of loss calculation error if strand-to-strand induced current decay time for particular cable is not known. Because of very low interstrand resistance Rutherford cable coupling losses can be very high dominating the dissipation among other components of losses.

- The proximity effect coupling can be reduced substantially by adding small amounts of Mn to the cooper matrix. Then proximity hysteresis near zero field becomes neglectable.

- Transport current distribution effects, flux penetration through the filaments saturated layer, eddy currents in the yoke, collar, and wedges are minor sources of dissipation and could be neglected. Mechanical hysteresis is also weak source of loss.

- The resistance under standard magnet prestress between adjacent strands is considerably lower than between non-adjacent strands (interstrand resistance anisotropy). The non-adjacent strand resistance can vary sometimes more than one order of magnitude from turn to turn, as well as in each particular turn of the magnet. The high ramp rate quench sites have lower interstrand resistances and a lower degree of interstrand resistance anisotropy.

- The interstrand resistance distribution in a magnet coil appears to be an unique function of the cable and coil technology and/or magnet assembly procedure. Interstrand resistance of Rutherford cables influences ramp rate quench current magnet characteristics as well as multipole decay time, i. e., the quality of magnetic field. Thus, the interstrand resistance strict control in order to make accelerator magnets with predictable characteristics could be a problem at mass production of magnets and a large scale application of superconductivity.

- The eddy current loss distribution in each particular turn of the magnet coil will depend on interplay between crossover, side-by-side and rollover resistances. It appears that crossover resistance plays the major role in both the quench current characteristics and the field quality during the ramp.

III. COOLING PROBLEMS OF INTERACTION REGIONS QUADRUPOLES IMMERSED IN SUPERFLUID HELIUM

We are going to consider the cooling problems at superfluid helium of superconducting accelerator magnets of collider interaction region reviewing characteristics of LHC (Large Hadron Collider) under construction at CERN. We also are going to discuss studies curried out at KEK (High Energy Accelerator Organization) of Japan which are relevant to it.

The LHC is designed to produce p–p collisions at center mass energy $E_{cm} = 14$ TeV and luminosity $L = 10^{34}$ cm^{-2}s^{-1}. The designed value of vacuum in the beam pipe is 10^{-9} Torr. The interaction rate of 8×10^8 s^{-1} represents a power of almost 900 W per beam, the large amount of which is directed towards the magnets of interaction region (the insertion magnets). The quadrupole field sweeps the secondary particles into the magnet coil preferentially along the vertical and horizontal planes, giving rise to local peak power density as much as an order of magnitude larger that the average one. Besides both the efficient 2 m long collimator system and the ticker beam tube in the interaction region (as scattered particles absorber) to be used each insertion quadrupole will receive additional $30 \div 35$ W heat power coming mainly from p–p scattering.

Actually there are two types of scattering: p–p and nuclear scattering with air. Since the probability for proton–air particles scattering is low the major source of beam scattering heat deposition is p–p collisions (Fig. 15). As an illustration locations of LHC ATLAS interaction region collimator, inner triplet quadrupoles, and beam separation dipoles as well as additional heat load coming from beam scattering are shown in Fig. 16. Such an additional heat load can cause serious operational problems for interaction region quadrupoles cooled by superfluid helium (1.9 K). For instance, it can increase the temperature of the coil above the λ-transition which immediately will overheat the superconductor above critical temperature because of much poorer heat transfer in He I than in He II. Quenching interaction region magnets will interrupt accelerator operation which is highly undesirable. In order to avoid that we are going to discuss what can be done to increase efficiency of cooling the magnet coil in superfluid helium.

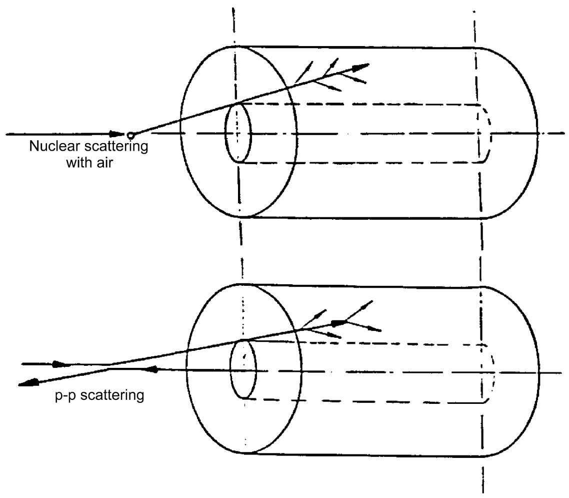

Fig. 15. Scattering occurring at interaction region; p–p scattering is the major source of additional beam loss heating.

Prior to that, however, we will remind to the reader basic heat transport properties of He II. In a bulk situation the viscosity of superfluid component of He II equals zero: $\eta_s = 0$. Viscosity of He II equals viscosity of the normal component: $\eta = \eta_n$. Density of He II is an additive of superfluid component density and normal component density: $\rho = (\rho_s + \rho_n)$, where the normal density to superfluid density ratio, ρ_n/ρ_s, is a strong function of temperature T given by

$$\frac{\rho_n}{\rho_s} = \left(\frac{T}{T_\lambda}\right)^{5.6} \quad \text{at} \quad T < T_\lambda \,, \tag{18}$$

and

$$\frac{\rho_n}{\rho_s} = 1 \quad \text{at} \quad T \geq T_\lambda \,. \tag{19}$$

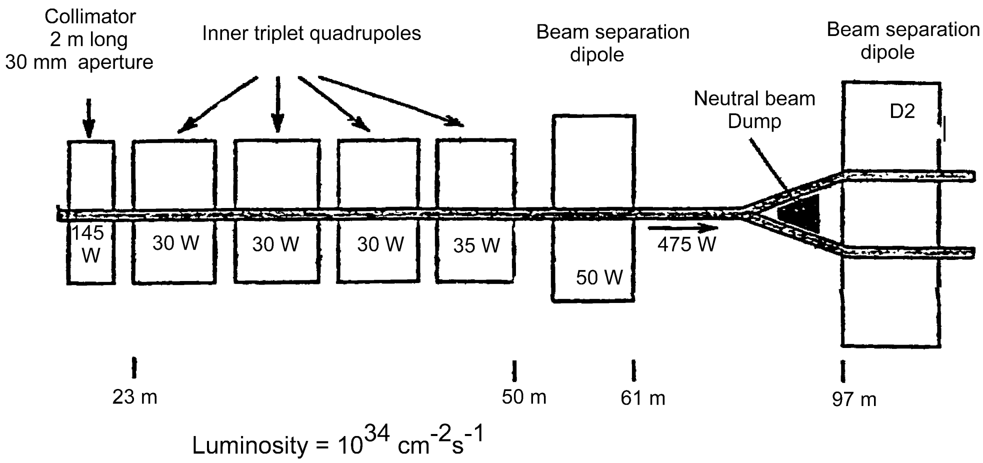

Fig. 16. Schematic of LHC ATLAS interaction region. Additional heat power load on the collimator, the insertion quadrupoles, and the separation dipoles are given in the figure.

In other words, at temperatures not much below λ-transition entire He II becomes superfluid. The entropy of superfluid component of He II equals zero: $S_s = 0$. Entropy of the entire He II equals normal component entropy: $S = S_n$. The momentum density of He II in a narrow channel (capillary) is

$$\mathbf{J} = \rho\mathbf{v} = \rho_s\mathbf{v}_s + \rho_n\mathbf{v}_n = 0 \,, \tag{20}$$

where $\mathbf{v}_s$ and $\mathbf{v}_n$ are the velocities of the superfluid and normal components, respectively. A momentum density equal to zero means that for any given cross-section of a capillary (Fig. 17) there is no mass transfer in a contraflow of superfluid and normal component of He II. In a thin capillary (approximately 1 μ in equivalent diameter) there is no perpendicular to the capillary axis component of velocity, i.e., there is no velocity reduction (prior to some critical value of velocity) of superfluid component along the capillary axis:

$$\nabla \times \mathbf{v}_s = 0 \quad \text{at} \quad v_s < v_{sc} \,. \tag{21}$$

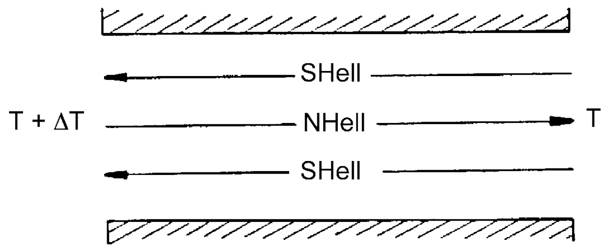

Fig. 17. Heat transport of He II in a channel.

In other words we have constant velocity of superfluid component in a thin capillary and we do not observe velocity dissipation typical for any viscous liquid. Heat transport properties of He II in a narrow channel can be summarized by considering Fig. 17 and Fig. 18. The temperature increase at one side of the channel (Fig. 17) causes normal component to flow in the center of the channel towards the lower temperature location. The same mass of superfluid component of He II goes around the channel walls in an opposite direction as a contraflow.

At relatively low heat flux q (Fig. 18) temperature increase ΔT *vs.* q is a straight line (Landau regime). The heat flux is given by

$$q = \frac{A}{L} d^4 \frac{(\rho S)^2 T}{12\eta_n} \Delta T \;, \tag{22}$$

where A is a constant, L is the length of the channel, and d is the equivalent diameter of the channel. In Landau regime there is no dissipation in superfluid/normal component counterflow. There is no interaction between thermal excitations of superfluid component and the normal one. There is no friction between two components of He II. This occurs till superfluid/normal component contraflow reaches a critical velocity that reflects to a critical heat flux (Fig. 18). Around the critical heat flow we have a transition regime and above the critical point the heat transport in He II follows the Gorter–Mellink law:

$$q^3 = \frac{A_0^3}{L} \int_{T_b}^{(T_b+\Delta T)} f^{-1}(T) dT \;, \tag{23}$$

where

$$f^{-1}(T) = \frac{A_{\mathrm{GM}}(T)\rho_n}{\rho_s S^4 T^3} \tag{24}$$

is the thermal conductivity of He II, A_0 is the effective cross section area of the cooling channel, A_{GM} is a Gorter–Mellink parameter.

Actually, $f^{-1}(T)$ is a function representing cooling efficiency of He II and it has a maximum with temperature. The cooling efficiency of He II pressurized at about 1 bar has a maximum at about 1.9 K and all superconducting devices to be cooled by He II are designed to operate at this temperature.

Curves 1 and 2 in Fig. 18 are for different channel (capillary) diameter d. The upper curve represents $\Delta T(q)$ for a channel with smaller diameter. As one can see smaller channel (capillary) has higher critical heat flux for the transition from Landau regime to Gorter–Mellink regime of heat transport. In Gorter–Mellink regime the heat flux *vs.* temperature difference is a cubic dependence. The thermal excitations in superfluid component of He II interact with normal component of He II which leads to friction in the contraflow and sharp increase of ΔT *vs.* heat flux.

Going back to cooling problems of interaction region quadrupoles of LHC we have to notice that the peak beam loss will produce about 8 mW/cm^3 additional heat power deposition to the inner coil itself. Because of different approaches to beam dissipation the loss calculations give different width of loss peak. Thus, we have conducted experiments simulating variety of heat load distribution.

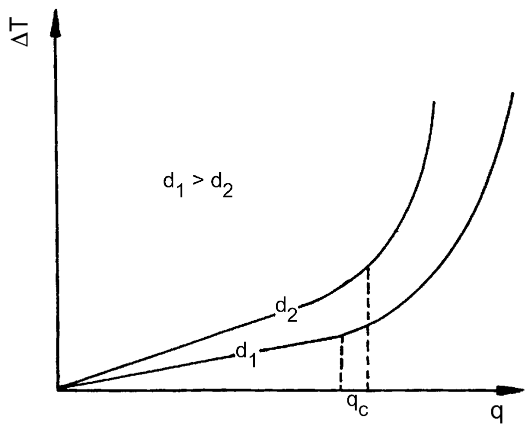

Fig. 18. Scheme of different regimes of heat transport in He II channels. Straight lines represent laminar counterflow of He II (Landau regime). Dashed lines indicate critical values of heat flux and the start of dissipation in the counterflow. Curves at higher heat flux represent Gorter–Mellink regime of heat transport in He II. The curve on the top represents the result for a channel with equivalent diameter, d_1, larger than the one for the curve shown at the bottom.

Early studies of additional beam loss problems of interaction region quadrupoles were performed at CEA, Saclay. For these experiments insulated stainless steel plates were used as samples [20]. We decided to use Rutherford cables with the same dimensions and keystone angle as superconducting one for LHC insertion quadrupoles but made of Cu–Ni strands and heated by transport current at zero field. This is much closer to reality having in mind that strands in a cable insulation encloses certain volume of helium due to some voids between strands.

The aim of these studies was to explore Rutherford cable samples and to find out insulation assuring better cooling for LHC interaction region quadrupoles. The sample preparation procedure is shown in Fig. 19.

The cable specimen (Fig. 19a) has two layers of an over-wrapped polyimide (upilex) tape and another polyimide tape pre-impregnated with epoxy resin wrapped around the cable specimen with $1 \div 3$ mm gap. After wrapping with insulation the cable specimens were cured into stacks shown on Fig. 19b using standard curing procedure [21]. One or several "thermometric" cables in a stack are surrounded by non-heated cables in order to reproduce conditions for different width of the beam loss peak.

Thermometric cables are cable specimens instrumented by thermometers, voltage and current leads, and heated by a transport current during measurements. Thermometers installed were CX–1030–BC, Lake Shore Cryotronic Inc. They were installed into tiny holes (shown on insertion of Fig. 19a) made by a special discharge method and then sealed by an epoxy resin with relatively high thermal conductivity at low temperature and not permeable to He II. The holes for thermometers are going deeply into the middle of cable specimens just in between two strands in order to avoid any non-symmetry of heating by the transport current. Two G10 caps were attached at both ends of cable stack specimens with Stycast epoxy to be free from the end effects due to longitudinal access of He II along the cable stack.

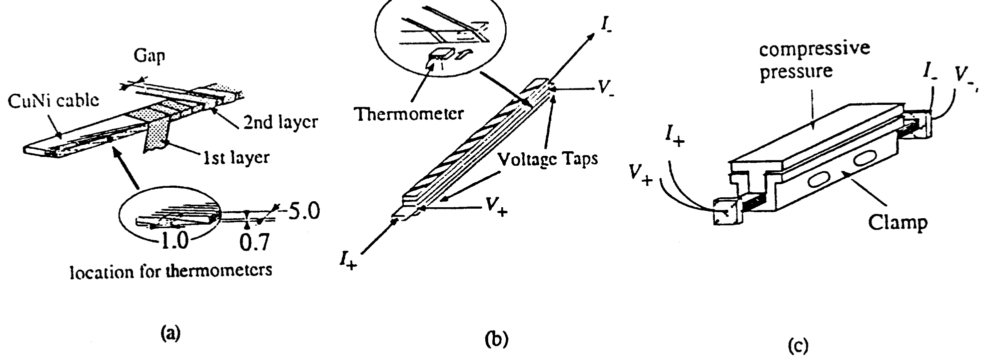

Fig. 19. Sample preparation procedure: (a) wrapping of two layers of insulation and thermometer location, (b) view of cable stack, thermometers installation and voltage taps location, (c) cable stack installed into compressive clamp.

The cryostat for these experiments shown schematically in Fig. 20 has an insulating plate (λ-plate) separating He II bath and 4.2 K helium bath. Three specimens were suspended simultaneously from λ-plate and were immersed in the He II bath. A heat exchanger with $J-T$ valve was equipped in the He II bath when experiments were performed under pressurized He II conditions. A pumping system was used to create saturated superfluid in He II bath. The vapor pressure in either the He II bath or the heat exchanger was controlled with a pressure control valve, V_1 (Fig. 20). The valve was connected to an absolute pressure transducer, P_1, through an electric feedback loop. The transducer was mounted on the cryostat at room temperature. The temperature of He II bath was kept constant between 1.65 K and 2.16 K with an accuracy of a few mK throughout the measurements by means of the control feedback loop system.

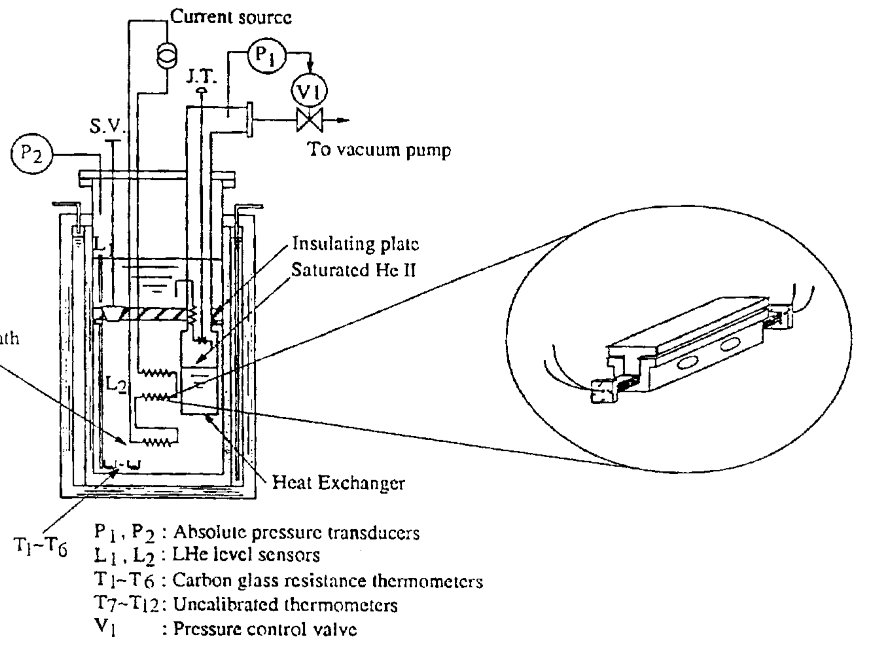

Fig. 20. Experimental set up for studying heat transport from Rutherford-type cables to He II. P_1 and P_2 are absolute pressure transducers. L_1 and L_2 are liquid He level sensors. T_1–T_6 are carbon glass resistance thermometers. T_7–T_{12} are CX thermometers. V_1 is pressure control valve.

Calibrated carbon glass resistance thermometers (CGR–1–500, Lake Shore Cryotronic Inc.) were used for obtaining He II bath temperature as well as for calibration of CX thermometers prior to each experimental run. Experimental data such as output voltage of thermometers, output voltage across the thermometric cables and output voltage of the shunt resister used to measure the heating transport current through thermometric cables were measured with three multichannel data recorders.

The data from the recorders were stored in a personal computer via GP–IB interface. The data acquisition system made it possible to measure the temperature difference between He II bath and the inside of cable stack within less than 5 mK.

We have done number of experiments in pressurized He II at different temperatures, in saturated He II and in He I. We have curried out experiments on different cable stacks (different number of thermometric cables in a stack) and various insulation materials. We have also collected data for different prestress on stacks, uncured samples, etc. The results are given in detail in Refs. [21–24] and we are not going to discuss it in this work. We can noticed only that cooling efficiency does not depend much on temperature of pressurized He II around 1.9 K, on prestress, on curing parameters or presence of epoxy absorbing material during curing.

Here we are going to discuss part of results obtained which we consider important for understanding a cooling performance in He II and we believe it can give a substantial impact for improving cooling characteristics of magnets. Before starting the discussion we would like to present results for $\Delta T(q)$ of two samples: cable and solid plate (Fig. 21). Someone can see substantial difference in cooling characteristics, which confirms the necessity of doing such experiments on Rutherford-type cables instead on solid plates as mentioned above.

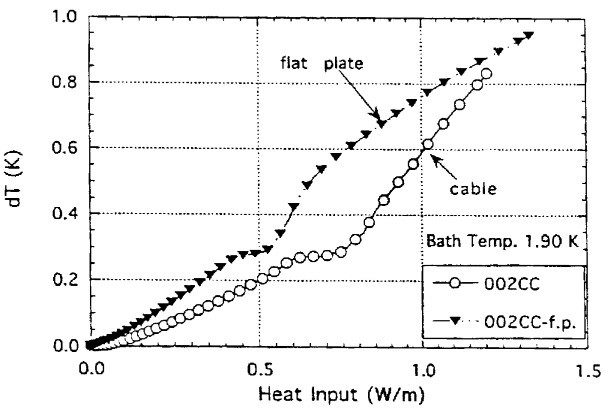

Fig. 21. Comparison of cooling efficiency at 1.90 K of Rutherford cable specimen (○ — 002CC) and plate specimen (▼ — 002CC–f.s.).

We were pretty surprised observing no difference in cooling characteristics of stack specimens containing cables with different gap of the second insulation layer (Fig. 22). We would expect noticeable improvement of cooling with the gap increase. A microscopic examination of samples has shown that 20 μ epoxy layer on the surface of the second insulation tape is too thick and the epoxy after polymerization (during curing of magnet coil) "seals" up drastically microchannels between the first and second layers of insulation reducing the effective heat transfer from the cable structure to the He II bath. This explains the previous result why cooling efficiency does not depend on second insulation layer gap (Fig. 22). The answer is: the amount of epoxy is so large that sealing of cooling channels after polymerization occurs with no difference from the width of second insulation gap we have.

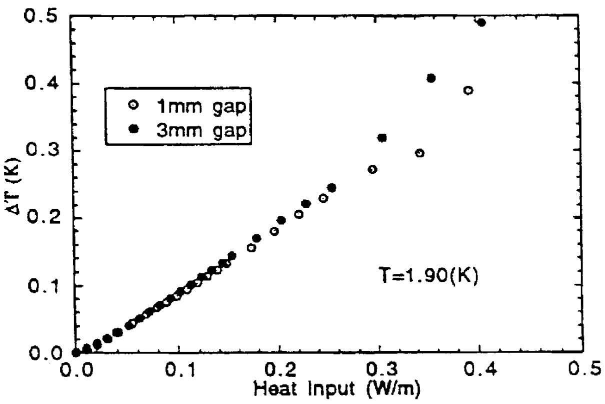

Fig. 22. Temperature difference *vs.* heat flux power input at T = 1.9 K for specimen with 1 mm second insulation layer gap (○ — 202AB) and specimen with 3 mm gap (● — 202AB1).

In order to verify above consideration, an uncured specimen with 20 μ epoxy tape was measured under the same bath conditions. The results for this stack of cables is not shown, however, the data were very close to those for thermally melted adhesive tape and no epoxy (Fig. 22). Obviously, the result confirms our assumption. Fig. 23 shows experimental ΔT *vs.* q characteristics for cured samples with 20 μ epoxy on the second layer of insulation, with 5 μ epoxy layer and with thermally adhesive tape with no epoxy. The insulation tape with reduced amount of epoxy (5 μ) was developed especially for this experiment. As one can see in Fig. 22, the reduction of epoxy thickness leads to an improvement of cooling characteristics. Samples made with no epoxy at all have the best cooling performance. The improvement of the cooling performance in comparison with the samples insulated by a standard 20μ epoxy tape is at least by a factor of two at a heat flux of the beam loss level.

We must notice here that many samples measured have shown a plateau of ΔT *vs.* q characteristics (see Fig. 23) in superfluid region just prior to λ-transition in helium. Samples with open cooling channels, i. e., with no epoxy, have the largest plateau. In some samples those plateaus are so large that the heat flux can be increased by a factor of 2 $\div$ 3 at practically constant ΔT. This was never mentioned in previous experiments [20, 25] and could not be explained by a normal liquid terms. An introduction of a new powerful cooling mechanism after classical Gorter–Mellink type of heat transport can be clearly seen on log–log plot of $\Delta T(q)$ data (Fig. 24).

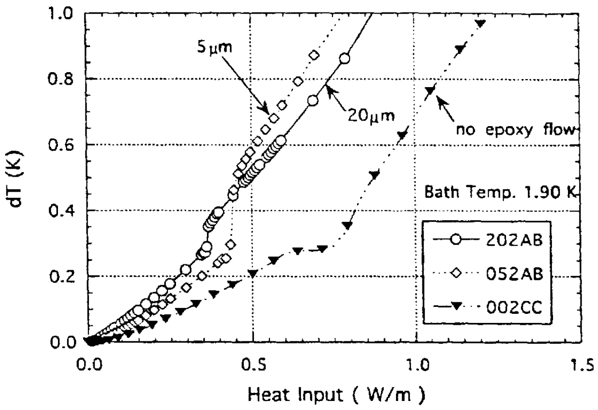

Fig. 23. Temperature difference *vs.* heat flux power input at 1.90 K. Data for specimen with 20 μ epoxy on the top of second layer of insulation are given by circles ($\circ$ — 202AB). Data for specimen with 5 μm epoxy are given by tilted empty squares ($\diamond$ — 052AB). Data for specimen with thermally adhesive tape are presented by black triangles ($\blacktriangledown$ — 002CC).

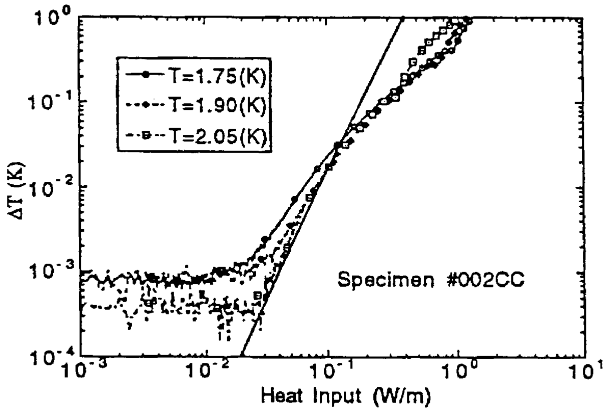

Fig. 24. Log–log plot of temperature difference *vs.* heat flux power input at 1.90 K for specimen with thermally adhesive insulation tape. The solid line represents $\Delta T \propto q^3$ dependence.

We consider the volume of He II between the cable strands and enclosed by the insulation to be connected with the He II bath via number of small randomly distributed, different in cross section and length cooling channels throughout the insulation. We consider that the equivalent diameter of these channels ranges from approximately 1 μ up to about 10 μ. As shown in Fig. 24 for one of our samples at low heat flux (about 0.02 W/m and below) ΔT is negligible and of the order of the sensitivity level of our measurements. Presumably, in this region we have laminar two-fluid flow heat exchange of Landau type, i. e., a linear dependence of ΔT *vs.* q. This is taking place in the channels with relatively large diameter (for instance, 10 μ). After reaching critical velocity in these channels (see in Fig. 24 heat input above 4×10^{-2} W/m) the heat transfer becomes of Gorter–Mellink type. One can clearly see that experimental points fit fairly well $\Delta T = q^3$ dependence (solid line in Fig. 24).

Above $0.15 \div 0.20$ W/m $\Delta T(q)$ starts to deviate from Gorter–Mellink behaviour. Obviously, another heat transfer mechanism becomes dominant. We assume that the cable insulation starts to perform as a superfluid filter. The superfluid component enters into the cable space through relatively small (about 1 μ in diameter) insulation channels permeable to the superfluid component only and a net mass flow exits the cable space via the channels previously providing the Gorter–Mellink type of heat transfer. Thus, we have He II forced flow heat transfer due to a kind of self sustained fountain pumping effect that we assume could be responsible for flattening of $\Delta T(q)$ dependence just below the λ-point. The forced flow heat transfer will become more effective with the increase of cable dissipation until a critical velocity in the channels supplying superfluid component is reached which presumably will cause a transition to He I heat transfer regime. For different specimens the plateau occurs at different heat input. We contribute that to the random properties of cable insulation as a superfilter. Obviously, an insulation that is sealed by epoxy resin containing no relatively small channels cannot perform as a superfilter and no plateau can be observed on $\Delta T(q)$ dependence (Fig. 23).

Section III conclusions

- $\Delta T(q)$ for specimens in the shape of Rutherford cables exhibit better cooling characteristics than those for solid plates at the same other He II parameters.

- The cooling efficiency of Rutherford-type cables is strongly affected by the amount of epoxy flow during curing. The excess of epoxy resin on the second layer of insulation seals cooling microchannels of insulation during curing of magnet coil (polymerization of epoxy under elevated temperature and pressure). Blocking cooling channels results in reduction of transported heat to He II bath and worsening of cooling characteristics of magnet coil. That reduction is undesirable especially for interaction region quadrupoles.

- Cables insulated with a second insulation layer with reduced amount of epoxy resin (for instance, 5 μ thick) give better cooling results than cables insulated by a standard one (20 μ thick epoxy layer).

- Best cooling characteristics are obtained for specimens with thermally melted adhesive tape containing no epoxy. This is obviously due to the lack of blockage of any cooling channels and better access of He II to the cable.

- Large plateau on experimental $\Delta T(q)$ dependence observed just below the λ-transition for many specimens presumably is due to forced flow of He II heat transfer caused by self-sustained fountain effect pumping. The latest is possible because the quantum mechanical behaviour of He II.

- More porous insulation of cables gives an opportunity for very efficient heat transfer from magnet coil to He II bath at the temperature just below the λ-transition.

- Utilizing fountain effect pumping for enhancement cooling efficiency of accelerator magnets by superfluid helium would give a chance for solving problems caused by additional beam loss heat load of interaction region quadrupoles.

ACKNOWLEDGEMENTS

The author would like to thank all his co-authors and colleagues for many years of joint efforts in superconducting magnet R&D.

Editor's note: The author has been involved for number of years in testing and analysis of superconducting materials, accelerator magnets, and magnets for thermonuclear devices in leading laboratories of USA and Japan.

[1] E. B. Forsyth, Science **242**, 391 (1988).
[2] G. Snitchler, R. Jayakumar, V. Kovachev, D. Orrell, *in: Supercollider 3*, edited by J. Nonte (Plenum Press, New York, 1991) p. 625.
[3] R. Jayakumar, V. Kovachev, D. Orrell, G. Snitchler, IEEE Trans. Magn. **28**, 148 (1992).
[4] Y. B. Kim, C. Hempstead, A. R. Strnad, Phys. Rev. **129**, 528 (1963).
[5] W. J. Carr, Jr., *AC Loss and Macroscopic Theory of Superconductors* (Gordon & Breech, New York, 1983)
[6] G. Morgan, J. Appl. Phys. **44**, 3319 (1973).
[7] G. T. Mallick. Jr., D. Natelson, W. J. Carr, Jr., G. Snitchler, V. Kovachev, IEEE Trans. Magn. **3**, 744 (1993).
[8] Y. Morita, K. Hara, N. Higashi, K. Hosoyama, A. Kabe, H. Kawabata, Y. Kojima, H. Nakai, T. Shintomi, A. Terashima, *Proceedings of the 16th ICEC/ICMC* (Elsevier Science Limited, UK, 1998) p. 1239.
[9] C. Haddock, V. Kovachev, D. Capone, *Proceedings of 1995 Particle Accelerator Conference and International Conference on High Energy Accelerators, Dallas, May 1–5, 1995,* p. 1417; IEEE Catalog 95CH35843 (1996).
[10] V. T. Kovachev, M. J. Neal, J. M. Seuntjens, J. T. Madison, S. O. Graham, P. G. Cline, M. Wake, D. W. Capone II, SSCL–Technical Report 637 (August, 1993).
[11] V. T. Kovachev, M. J. Neal, J. M. Seuntjens, J. Qin, P. G. Cline, C. Swenson, D. W. Capone II, SSCL–Technical Report 651 (November, 1993).
[12] M. J. Neal, V. T. Kovachev, SSCL–Technical Report 666 (March, 1994).
[13] V. T. Kovachev, M. J. Neal, D. W. Capone II, W. J. Carr, Jr., C. Swenson, Cryogenics **34**, 813 (1994).
[14] W. J. Carr, Jr., V. T. Kovachev, Cryogenics **35**, 529 (1995).
[15] G. T. Mallick, Jr., W. J. Carr, Jr., J. M. Toms, V. T. Kovachev, Cryogenics **35**, 653 (1995).
[16] G. T. Mallick, Jr., W. J. Carr, Jr., H. L. Chuboy, D. Marschik, J. M. Toms, V. T. Kovachev, Westinghouse STC preprint, Pittsburgh, September 30, 1994.
[17] W. J. Carr, Jr., V. T. Kovachev, Westinghouse STC preprint, Pittsburgh, August 3, 1994.
[18] W. J. Carr, Jr., J. T. Mallick, V. T. Kovachev, Westinghouse STC preprint Pittsburgh, September 12, 1994.
[19] T. Ogitsu, A. Devred, V. Kovachev, Particle Accelerators **57**, 215 (1997).
[20] C. Meuris, Cryogenics **31**, 624 (1991)
[21] N. Kimura, V. Kovachev, T. Nakamoto, A. Yamamoto, T. Shintomi, A. Terashima, K. Tanaka, T. Haruyama, *Adv. Cry. Eng.*, edited by P. Kittel (Pleanum Press, New York, 1998) p. 1433.
[22] N. Kimura, A. Yamamoto, T. Shintomi, A. Terashima, V. Kovachev, M. Murakami, IEEE Trans. Appl. Supercond. **9**, 1097 (1999)
[23] A. Yamamoto, T. Nakamoto, A. Terashima, E. Burkhardt, N. Higashi, H. Kawamata, N. Kimura, V. Kovachev, T. Ogitsu, N. Ohuchi, T. Shintomi, K. Tanaka, K. Tsuchiya, G. A. Kirby, R. Ostojic, T. M. Taylor, *Proceedings of the 15th International Conference of Magnet Technology, part 1* (Science Press, Beijing, China, 1998) p. 59.
[24] N. Kimura, V. Kovachev, T. Nakamoto, A. Yamamoto, T. Shintomi, A. Terashima, K. Tanaka, T. Haruyama, *Proceedings of the 15th International Conference of Magnet Technology, part 2* (Science Press, Beijing, China, 1998) p. 1238.
[25] B. Baudouy, A. Boucheffa, M. X. Francois, C. Meuris, *Proceedings of the 16th ICEC/ICMC* (Elsevier Science Limited, UK, 1998) p. 563.

ПРО ДЕЯКІ ПРОБЛЕМИ ВЕЛИКИХ НАДПРОВІДНИХ МАГНЕТІВ

В. Ковачев
Інститут фізики твердого тіла ім. Ґ. Наджакова
Болгарська академія наук, BG–1784, Софія, Болгарія

Перша частина огляду присвячена неточностям аналітичних та числових аналізів дисипації енерґії в надпровідних магнетних прискорювачах, що працюють при відносно високих темпах. Обговорено неточності експерименту, а також джерела похибок при вимірюваннях. Розглянуто кореляцію між міжпучковим опором структур Резерфорда та поведінкою послаблення струму надпровідних магнетів. У другій частині цього огляду подано деякі важливі проблеми охолодження введених квадруполів для великого адронного колайдера (CERN). Експериментальні результати при температурі, нижчій за 2 K, проінтерпретовано за допомогою можливого самопідтримуваного накачування, базованого на квантовомеханічному фонтанному ефекті в надплинному ^{4}He.